

Spectrally resolve flux derived from collocated AIRS and  
CERES observations and its application in model validation,

Part I: clear-sky over the tropic oceans

Xianglei Huang<sup>1\*</sup>, Wenze Yang<sup>1</sup>, Norman G. Loeb<sup>2</sup>, V.  
Ramaswamy<sup>3</sup>

1. Department of Atmospheric, Oceanic, and Space Sciences, University of Michigan,  
Ann Arbor, MI 48109-2143
2. Radiation and Climate Branch, NASA Langley Research Center, Hampton, Virginia
3. Geophysical Fluid Dynamics Laboratory, NOAA, Princeton University Forrestal  
campus, Princeton, New Jersey

\* Corresponding author: Dr. Xianglei Huang, Department of Atmospheric, Oceanic, and  
Space Sciences, 2455 Hayward Street, University of Michigan, Ann Arbor, MI  
48109-2143 xianglei@umich.edu, (734) 936-0491

To be submitted to *Journal of Geophysical Research-Atmospheres*

June 26, 2007

## **Abstract**

Spectrally resolved outgoing IR flux, the integrand of the outgoing longwave radiation (OLR), has its unique value in evaluating model simulations. Here we describe an algorithm of deriving such clear-sky outgoing spectral flux through the whole IR region from the collocated Atmospheric Infrared Sounder (AIRS) and the Clouds & the Earth's Radiant Energy System (CERES) measurements over the tropical oceans. Based on the scene types and corresponding angular distribution models (ADMs) used in the CERES Single Satellite Footprint (SSF) dataset, spectrally-dependent ADMs are developed and used to estimate the spectral flux at each AIRS channel. A multivariate linear prediction scheme is then used to estimate spectral fluxes at frequencies not covered by the AIRS instrument. The whole algorithm is validated using synthetic spectra as well as the CERES OLR measurements.

Using the GFDL AM2 model simulation as a case study, the application of the derived clear-sky outgoing spectral flux in model evaluation is illustrated. By comparing the observed and simulated spectral flux in 2004, compensating errors in the simulated OLR from different absorption bands can be revealed, so does the errors from frequencies within a given absorption band. Discrepancies between the simulated and observed spatial distributions and seasonal evolutions of the spectral fluxes at different spectral ranges are further discussed. The methodology described in this study can be applied to other surface types as well as cloudy-sky observations and corresponding model evaluations.

## **1. Introduction**

As an entity, the global mean outgoing longwave flux (commonly known as outgoing longwave radiation, hereafter OLR) reflects how our climate system attempts to balance the net incoming solar radiation at the top of atmosphere (TOA). Being one type of energy flux, OLR consists of an integrated contribution of radiance intensities at different frequencies and from different directions, which in turn is determined by various atmospheric and surface parameters such as atmospheric temperature and humidity profiles, trace gas concentrations, surface temperature and emissivity, as well as clouds and aerosols. Owing to these facts, OLR has been long recognized by the climate community as an important quantity to observe and simulate [Allan, *et al.*, 2004; Barkstrom, 1984; Harries, *et al.*, 2005; Ramanathan, *et al.*, 1989; Wielicki, *et al.*, 1996; Wielicki, *et al.*, 2002]. Since the launch of ERBE (Earth Radiation Budget Experiments) satellites in mid-1980s [Barkstrom, 1984], there have been numerous studies of using the broadband OLR measured by ERBE in evaluating general circulation models (GCMs), operational analysis and reanalysis product [Allan, *et al.*, 2004; Raval, *et al.*, 1994; Slingo, *et al.*, 1998; Slingo and Webb, 1992; Wielicki, *et al.*, 2002; Yang, *et al.*, 1999]. Meanwhile, the integrand of OLR—the spectrally resolved radiance intensity—has not been used as much as the broadband OLR in such studies primarily because of a lack of measurements.

The spectrally resolved radiance has a unique value in evaluating climate models [Goody *et al.*, 1998]. So does the spectral flux. Using broadband observations to understand model deficiencies sometimes is not straightforward: individual model errors that contribute to the different spectral regions can compensate one another to make the

understanding of the whole broadband deficiencies difficult. From this aspect, it is obvious that spectrally-resolved quantities (radiance intensities or fluxes) are valuable in such evaluations. A recent study by *Huang et al.* [2006] illustrated how spectrally resolved radiances can be used to quantify the model bias previously seen from a comparison between the ERBE-observed and model-simulated clear-sky broadband OLR (hereafter, OLRc). By comparing simulated spectra with IRIS (Infrared Interferometer Spectrometer) spectra collected during April 1970-January 1971, they disclosed compensating errors from different absorption bands in the OLRc simulated by AM2, the new GFDL atmospheric GCM. Bias originating from the stratosphere can be also identified by examining infrared channels primarily sensitive to the stratospheric emissions. The IRIS dataset covers only a period of 10 months with sparse spatial sampling. Nevertheless, because auxiliary information about each individual IRIS footprint is not available, *Huang et al* [2006] had to use a single statistical regression scheme to do the radiance-to-flux conversion for all IRIS clear-sky spectra. Due to these limitations, *Huang et al* [2006] had to focus mostly on the bias of the monthly-mean clear-sky OLR averaged over the whole tropical ocean.

The Atmospheric Infrared Sounder (AIRS) [*Aumann, et al.*, 2003; *Chahine, et al.*, 2006] and the Clouds and the Earth's Radiant Energy System (CERES) [*Wielicki, et al.*, 1996] aboard NASA Aqua satellite provide a great opportunity of advancing the application of such spectrally resolved observations in model evaluations. The AIRS instrument records IR spectra over a wide spectral range while the CERES can provide measurements of the

broadband OLR. In order to convert unfiltered radiance to the broadband OLR, the CERES team has categorized individual footprints to different scene types and developed sophisticated angular distribution model (ADM) for each scene type [Loeb, *et al.*, 2005; Loeb, *et al.*, 2003]. This greatly facilitates the estimation of spectral flux at each AIRS channel since the CERES scene type information can be directly used to construct appropriate ADM for each AIRS channel. Since AIRS does not have a full coverage of the whole IR region, the broadband OLR estimated from the AIRS radiances can then be validated against the collocated CERES OLR. Moreover, the AIRS and CERES on Aqua has been collecting data since July 2002. AIRS records ~2.9 million spectra per day and the CERES instrument in the cross-track scan mode alone obtains ~2.4 million measurements per day. Such dense sampling patterns imply that, besides the monthly-mean spectral flux over a broad climate zone, detailed spatial distributions and temporal evolutions of the spectral flux can be examined and compared with model simulations. Moreover, with spectral fluxes derived for both all-sky and clear-sky observations, band-by-band longwave cloud radiative forcing (LW CRF, the difference between clear-sky and all-sky flux) at the TOA can be obtained. Such spectrally-dependent cloud radiative forcing can be used as a more stringent metric to assess the simulation of clouds in the GCMs

The focus of this study is the clear-sky outgoing spectral flux over the tropical oceans and its application in model evaluation. The derivations of cloudy-sky spectra flux and hence band-by-band longwave cloud radiative forcing, as well as their applications in

model evaluation, will be presented in a separate study. The rest sections are organized in the following way. Section 2 describes the datasets and models used in this study. The algorithm for deriving spectral flux over the whole IR region from the collocated AIRS and CERES observations is depicted in section 3. Validation of this algorithm is discussed in section 4. Section 5 presents a case study how the derived spectral flux can be used in evaluating GCM simulations. Conclusions and further discussions are given in section 6.

## **2. Datasets and models**

### **2.1 CERES**

The NASA *Aqua* spacecraft carries two identical CERES instruments (FM3 and FM4) [Parkinson, 2003]. *Aqua* is in a sun-synchronous orbit 705km above the surface. The instrument field of view (IFOV) of CERES is about 1.63 degree, corresponding to a 20km nadir-view footprint on the surface. At any given time, one CERES instrument is placed in a cross-track scanning mode and the other in either a rotating azimuth scanning or a programmable azimuth plane mode. Given that AIRS is operating in a cross-track scan mode, only CERES observations from the cross-track scanning mode are used in this study. The CERES instruments measure filtered radiances in the shortwave (SW, 0.3-5 $\mu$ m), total (0.3-200 $\mu$ m), and window (WN, 8-12 $\mu$ m) regions. The filtered radiances are then converted to unfiltered reflected solar, unfiltered LW and WN radiances [Loeb et al., 2001]. Corresponding fluxes are derived based on these unfiltered radiances and corresponding angular distribution models (ADMs).

The CERES dataset used in this study is the *Aqua*-CERES level2 footprint data

product, the Single Satellite Footprint (SSF) TOA/Surface Fluxes and Clouds Edition 2A [Loeb, *et al.*, 2005]. The CERES SSF broadband fluxes are obtained from directional radiance measurements using a new generation of angular distribution models (ADMs) [Loeb, *et al.*, 2005; Loeb, *et al.*, 2007]. For the clear-sky over the oceans, the scene type of interest in this study, it is further stratified into discrete intervals of precipitable water retrieved from SSM/I (Special Sensor Microwave Imager) [Goodberlet, *et al.*, 1990], vertical temperature change in the first 300hPa of the atmosphere above the surface as derived from GEOS Data Assimilation System [DAO, 1996], and image-based surface skin temperature. ADM is constructed for each discrete interval. Using these ADMs significantly reduces both the bias and the root-mean-square (RMS) errors of LW TOA flux. Loeb *et al.* [2007] estimated a bias of 0.2-0.4 Wm<sup>-2</sup> and RMS error < 0.7 Wm<sup>-2</sup> for Aqua-CERES regional mean LW TOA flux.

## 2.2 AIRS and the collocation strategy

AIRS is an infrared grating array spectrometer aboard *Aqua* [Aumann, *et al.*, 2003]. It records spectra at 2378 channels across three bands (3.74-4.61μm, 6.20-8.22μm, 8.8-15.4μm) with a resolving power ( $\lambda/\Delta\lambda$ ) of 1200. AIRS scans from -49° to 49° with an IFOV of 1.1 degree, corresponding to a nadir-view footprint of 13.5km on the surface. The in-flight calibrations show a radiometric accuracy of < 0.3K for a 250K brightness temperature target [Pagano, *et al.*, 2003] and a spectral accuracy of < 0.01Δν (Δν here is the full width at half maximum of each channel) [Gaiser, *et al.*, 2003]. AIRS collects ~2.9 million spectra per day and global coverage can be obtained in the course of 2 days. It

provides an unprecedented data source of the outgoing thermal IR spectra with excellent calibration and good global coverage.

In this study we use the AIRS geo-located and calibrated radiances (level 1B). Among the 2378 AIRS channels, only those recommended by the AIRS team for level-2 retrieval purposes are used. Given that CERES LW flux is defined as flux over 0-2000  $\text{cm}^{-1}$ , AIRS radiances in 3.74-4.61  $\mu\text{m}$  (2169-2673  $\text{cm}^{-1}$ ) band are not used in this study. In addition, we screen the data with a strict quality control procedure to exclude possible bad spectra as did in *Huang & Yung* [2005].

Figure 1 shows part of AIRS and CERES FM4 (in cross-track scanning mode) footprints as sampled from 01:06UTC to 01:12UTC on January 01, 2005. The area of an AIRS footprint is about 45% of that of CERES footprint. As a result, many AIRS footprints are either completely or largely overlapped within corresponding CERES footprints. As we shall see in later sections, such overlapped measurements—a subset of both AIRS and CERES data—could still render meaningful gridded regional products. When an AIRS pixel that is completely within a CERES footprint, the scene type information of the CERES footprint and relevant auxiliary information stored in CERES SSF products can be directly applied to the AIRS pixel. Therefore, such collocation greatly facilitates the conversion from the AIRS radiances to spectral fluxes. The collocation criteria adopted in this study are (1) the time interval between AIRS and CERES observations is within 8 seconds, and (2) the distance between the center of AIRS footprint and that of CERES footprint on the surface ( $\Delta_{\text{airs-ceres}}$ ) is less than 3km. The



second criterion ensures the major portion of AIRS footprint is within the collocated CERES footprint even the scan angle becomes large enough. For example, at a scan angle of  $45^\circ$  and  $\Delta_{\text{airs-ceres}}=3\text{km}$ , an AIRS footprint still has at least 50% overlapping with the collocated CERES footprint. In practice, we only use AIRS data with scan angles within  $\pm 45^\circ$ .

### 2.3 Models

In order to construct ADMs suitable for the AIRS and estimate spectral fluxes at frequencies not covered by the AIRS instrument, a forward radiative transfer model is needed. We use MODTRAN<sup>TM</sup>-5 version 2 revision11 (Mod5v2r11) for this purpose. MODTRAN<sup>TM</sup>-5 was collaboratively developed by Air Force Research Laboratory and Spectral Sciences Inc [Berk, *et al.*, 2004]. Mod5v2r11 is based on HITRAN2K line compilation with updates through 2004 [Rothman, *et al.*, 2005; Rothman, *et al.*, 1998]. Compared to previous versions of MODTRAN band model [Berk, *et al.*, 1998; Bernstein, *et al.*, 1996], MODTRAN5 inherits the flexibility in handling clouds and significantly improves the spectral resolution to as fine as  $0.1\text{cm}^{-1}$ . Comparisons between this model and line-by-line radiative transfer model, LBLRTM [Clough and Iacono, 1995; Clough, *et al.*, 2005], show agreement up to a few percent or better in the thermal IR transmittances and radiances [Anderson *et al.*, 2006]. These features make MODTRAN5 well suited for simulating AIRS radiances [Anderson, *et al.*, 2006; Feldman, *et al.*, 2006]. In this study, synthetic AIRS spectrum is done by convolving the MODTRAN5 output at  $0.1\text{cm}^{-1}$  resolution with the spectral response functions of individual AIRS channels [Strow, *et al.*,

2006; *Strow, et al.*, 2003],

For illustrating the application of derived spectral fluxes in model evaluation, we use a version of AM2 (am2p14), the atmospheric GCM recently developed at NOAA Geophysical Fluid Dynamics Lab (GFDL). It employs a hydrostatic, finite volume dynamical core with  $2.5^\circ$  longitude by  $2^\circ$  latitude horizontal resolution and 24 vertical levels, the top level being at  $\sim 3$ hPa. Cloud quantities such as cloud liquid water, cloud ice amount, and cloud fraction are treated as prognostic variables. The relaxed Arakawa-Schubert scheme is used for cumulus parameterization with several modifications. The shortwave and longwave radiation parameterizations follow *Freidenreich & Ramaswamy* [1999] and *Schwarzkopf & Ramaswamy* [1999], respectively. The longwave radiation parameterization computes radiative fluxes at eight spectral ranges. The TOA flux at each spectral range can be directly evaluated against the counterparts derived from the collocated AIRS and CERES observations. A detailed description of AM2 can be found in *GFDL GAMDT* [2004].

The AM2 model are forced by observed monthly SSTs from 2002-2006. Ozone is prescribed at its 1990's level based on a combined dataset of observed stratospheric [*Randel and Wu*, 2007] and simulated tropospheric [*Horowitz*, 2006] ozone distributions. Observed CO<sub>2</sub> and other greenhouse gas concentrations appropriate for the period are used in the run. 3-hourly instantaneous outputs are archived from the simulation. To minimize the temporal sampling difference from the collocated AIRS-CERES dataset, the 3-hourly instantaneous output are further sampled to the same time and location as those collocated

AIRS-CERES observations identified in section 2.2. Besides the radiative fluxes over eight spectral ranges directly output from the AM2 model, the sub-sampled temperature and humidity profiles are fed into the MODTRAN5 to obtain spectral fluxes at every  $10\text{cm}^{-1}$  intervals from  $10\text{-}2000\text{ cm}^{-1}$ . Such  $10\text{cm}^{-1}$  spectral flux will also be compared with the counterpart derived from the collocated AIRS and CERES measurements.

### 3. Algorithm

Since we are interested in using AIRS observations to derive the spectral fluxes over the whole IR region, two issues have to be addressed: (1) estimating the spectral flux at each AIRS channel and (2) estimating the spectral fluxes at frequencies not covered by the AIRS instrument. Subsection 3.1 and 3.2 describe solutions to the two issues, respectively.

#### 3.1 Spectrally-dependent ADMs

Angular distribution model is needed to covert directional radiance measurement to flux. The central quantity in such conversion is the anisotropic factor, which is defined as

$$R_\nu(\theta) = \frac{\pi I_\nu(\theta)}{F_\nu} \quad (1)$$

where  $I_\nu(\theta)$  is the TOA upwelling radiance at frequency  $\nu$  along zenith angle  $\theta$ ,  $F_\nu$  is the TOA upwelling spectra flux at frequency  $\nu$ . Compared to the broadband anisotropic factor used in CERES ADMs,  $R$  here is not only a function of  $\theta$  but  $\nu$ .

Figure 2a shows  $R_\nu(\theta)$  of the United States 1976 standard atmosphere profile computed by the MODTRAN5 with a spectral resolution of  $2\text{cm}^{-1}$  for two zenith angles,  $0^\circ$  and  $60^\circ$ , respectively. It can be seen that  $R_\nu(\theta)$  has strong spectral dependence. For the

both angles, the anisotropic factors in the atmospheric window regions ( $850\text{-}1000\text{cm}^{-1}$ ,  $1100\text{-}1200\text{cm}^{-1}$ ) and the water vapor pure rotational band ( $< 500\text{cm}^{-1}$ ) are closer to one than those in other bands. For  $0^\circ$  zenith angle (the solid line in Figure 2a), the ozone band ( $990\text{-}1070\text{cm}^{-1}$ ), the Q-branch of methane band ( $\sim 1306\text{cm}^{-1}$ ), and the water vapor  $\nu_2$  band ( $1200\text{-}2000\text{cm}^{-1}$ ) tends to have  $R_\nu(\theta)$  noticeably larger than one. Meanwhile, at the center of the  $\text{CO}_2$  band ( $\sim 667\text{cm}^{-1}$ ),  $R_\nu(\theta)$  is smaller than one. For  $60^\circ$  zenith angle (dash line in Figure 2a), opposite cases can be seen in these bands. The contrast between the  $\text{CO}_2$  band and other bands is primarily due to the fact that the effective emission levels for channels at the  $\text{CO}_2$  band center locate in the stratosphere rather than in the troposphere. The larger the zenith angle ( $\theta$ ), the higher the effective emission level is. As temperature increases with the height in the stratosphere, this leads to a larger radiance intensity when  $\theta$  becomes larger. Therefore, if we define the frequency-dependent diffusive angle,  $\theta_{diff}$ , as  $\pi I_\nu(\theta_{diff}) = F_\nu$ . For any  $\theta < \theta_{diff}$ ,  $R_\nu(\theta)$  will be smaller than one; For any  $\theta > \theta_{diff}$ ,  $R_\nu(\theta)$  will be larger than one. In the troposphere, temperature decrease with the altitude, which means the opposite dependence of  $R_\nu(\theta)$  on  $\theta$ . To support our explanation, Figure 2b shows the  $R_\nu(\theta)$  for the upwelling flux at 9km altitude, which is within the troposphere instead of at the TOA. For this case, the  $\text{CO}_2$  band behaves similarly to other absorption bands, with  $R_\nu(0) > 1$  and  $R_\nu(60) < 1$ .

As mentioned in section 2.1 and 2.2, necessary scene type information can be retrieved from the CERES SSF product and then the scene type is directly applicable to the collocated AIRS observation. According to Table 3 in *Loeb et al.* [2005], clear-sky

conditions over all surface type are further stratified to 80 discrete intervals of precipitable water ( $pw$ ), lapse rate ( $\Delta T$ ), and surface skin temperature ( $T_s$ ). In practice, it turns out that only 14 out of the 80 intervals are needed to accommodate all possible clear-sky scenes observed over the oceans, which are listed in details in Table 1. Since in this study we focus on tropical ocean region, we only need to construct appropriate spectral ADMs for the 14 intervals.

We use 6-hourly profiles from the ECMWF ERA-40 reanalysis [Uppala, *et al.*, 2005] in conjunction with the MODTRAN5 to derive the spectral ADMs for all 14 intervals in the following way. Four months of ECMWF data (2001 October, 2002 January, 2002 April, and 2002 July) are used. For each month, four 6-hourly time intervals are chosen. For each selected 6-hourly period, temperature and humidity profiles between 60°S-60°N oceans are fed into the MODTRAN5 to compute anisotropic factors of individual AIRS channels for zenith angles from 0° to 45°. By doing so, 80,640 profiles and associated synthetic AIRS spectra and anisotropic factors are archived. Then these profiles and anisotropic factors are categorized into the discrete intervals of  $pw$ ,  $\Delta T$ , and  $T_s$  as listed in Table 1. The mean anisotropic factor from all samples belonging to an discrete interval is defined as the anisotropic factor for that interval. By doing so, spectrally-dependent ADMs for converting AIRS radiances to spectra fluxes are constructed.

The Aqua-CERES clear-sky LW broadband anisotropic factors are constructed from a sample space different from what is used here [Loeb *et al.*, 2005]. Moreover, for each discrete interval, the SSF product uses a pair of slightly different (~0.1% difference in

fraction) anisotropic factors, one for the daytime scenes and the other for the nighttime scenes. Figure 3 shows a pair of such CERES anisotropic factors for a given discrete interval (the gray solid lines with diamonds and circles). The corresponding broadband anisotropic factors derived from the aforementioned procedure are also shown in Figure 3 (black dash line). The three curves closely follow each other with minute differences. To reduce the contribution of such minute differences in ADMs to the differences in later comparisons between AIRS-derived broadband OLR and the CERES OLR, we define a scaling factor for each discrete interval,

$$s = \frac{R_{CERES}(\theta)}{R_{MODTRAN}(\theta)} \quad (2)$$

where  $R_{CERES}(\theta)$  is the LW broadband anisotropic factor used in the CERES SSF product (daytime or nighttime) and  $R_{MODTRAN}(\theta)$  is the counterpart derived from the aforementioned procedure. The spectrally-dependent anisotropic factors are then multiplied by this scaling factor. As far as the broadband OLR are concerned, such scaling ensures the consistency between our spectrally-dependent ADMs and the corresponding CERES LW broadband ADMs.

### 3.2 Estimating spectral fluxes at frequencies not covered by AIRS

In order to obtain spectral fluxes over the whole IR region, a scheme has to be developed to estimate spectral fluxes at frequencies without the AIRS coverage. AIRS has no coverage at frequencies lower than  $649.6\text{cm}^{-1}$  and between  $1613.9\text{-}2000\text{cm}^{-1}$ . AIRS has 12 modules assembled on the focal plane [Aumann *et al.*, 2003], each having its own

spectral range. The spectral ranges of neighbor modules might overlap with each other. As a result, a few spectral ranges are sampled by more than one module. Meanwhile, the modules do not provide a continuous coverage from  $649.6 \text{ cm}^{-1}$  and  $1613.9 \text{ cm}^{-1}$ . For example, no AIRS channel covers  $1136.6\text{-}1217.0 \text{ cm}^{-1}$  and  $1046.2\text{-}1056.1 \text{ cm}^{-1}$ . To address the spectral coverage issue, following strategy is adopted to cover the whole LW region ( $10\text{-}2000\text{cm}^{-1}$ ):

- (a) For the spectral range continuously covered by AIRS, AIRS channel frequency is used. For the spectral range sampled by two overlapped channels, only one channel is kept and used in later analysis.
- (b) Frequency gaps between  $649.6 \text{ cm}^{-1}$  and  $1613.9 \text{ cm}^{-1}$  are filled with channels having the same spectral resolution as the nearest AIRS channels.
- (c) For spectral region less than  $649.6 \text{ cm}^{-1}$ , it is filled with channels having a spectral resolution of  $0.5 \text{ cm}^{-1}$ , approximately the resolution at the nearest AIRS channel.
- (d) For spectral region between  $1613.9 \text{ cm}^{-1}$ - $2000\text{cm}^{-1}$ , it is filled with channels having a spectral resolution of  $1.5 \text{ cm}^{-1}$ , approximately the resolution at the nearest AIRS channel.

By making such choice of channels, the whole thermal-IR region is covered. As long as the spectral flux of each channel can be estimated based on AIRS radiances, the broadband OLR and the fluxes over individual spectral ranges can be calculated. Hereafter, above four sets of channels are referred as channel sets (a)-(d), respectively.

For AIRS channels, the channel set (a), its radiance  $I_\nu(\theta)$  can be converted to the spectral flux  $F_\nu$  using the spectrally-dependent ADMs described in section 3.1. For channels in the sets of (b)-(d), a multi-regression scheme based on the Principal Component Analysis is used to obtain the corresponding spectra fluxes. Parameters in the regression scheme are derived based on the ECMWF profiles and synthetic spectra mentioned in section 3.1. In details, for every ECMWF profile falling into a given discrete interval of  $(pw, \Delta T, T_s)$ , the synthetic spectral fluxes at all channels set (a)-(d) are computed. Spectral EOF analysis (principal component analysis in the spectral domain) [Haskins, et al., 1999; Huang, et al., 2003; Huang and Yung, 2005] is applied to the collection of synthetic spectral fluxes to derive a set of orthogonal basis in the frequency domain,

$$F_\nu = \bar{F}_\nu + \sum_{j=1}^N e_j \phi_\nu^j \quad (3)$$

where  $F_\nu$  is synthetic spectral flux at frequency  $\nu$  from one ECWMF profile,  $\bar{F}_\nu$  is the average of all synthetic spectral fluxes at  $\nu$ .  $N$  is the total number of channels,  $\phi_\nu^j$  ( $j=1-N$ ) are the principal components (unit vectors) that consist of a complete set of orthogonal basis in the  $N$ -dimensional space, and  $e_j$  is the projection of  $(F_\nu - \bar{F}_\nu)$  onto the  $j$ -th principal component  $\phi_\nu^j$ . In practice, it is found that 99.99% variance can be explained by the first 20 or even less principal components. Therefore, we only retain the first  $M$  principal components that account for 99.99% variance. In the matrix form, it means



$$\mathbf{F} - \bar{\mathbf{F}} \approx [\phi^1, \phi^2, \dots, \phi^M] \begin{bmatrix} e_1 \\ e_2 \\ \dots \\ e_M \end{bmatrix} = \Phi \mathbf{e} \quad (4)$$

where  $\mathbf{F}$ ,  $\bar{\mathbf{F}}$ ,  $\phi^1$ , ...,  $\phi^M$  are vectors with a dimension of  $N$  ( $N \gg M$ ). Correspondingly,  $\Phi$  is an  $N \times M$  matrix and  $\mathbf{e}$  is an  $M \times 1$  vector. Note the total number of channels in channel sets of (a)-(d) is  $N$ . The total number of AIRS channels ( $N_{AIRS}$ ) is smaller than  $N$  but much larger than  $M$ .

Since (4) holds for all channels, if we use AIRS in subscript to denote a set of valid AIRS channels, we still have

$$\mathbf{F}_{AIRS} - \bar{\mathbf{F}}_{AIRS} \approx \Phi_{AIRS} \mathbf{e} \quad (5)$$

Note  $\mathbf{F}_{AIRS}$  could be derived from AIRS measurement as described in section 3.1.  $\bar{\mathbf{F}}_{AIRS}$ , on the other hand, are the mean spectral fluxes at the AIRS channels derived from the set of synthetic spectra mentioned before. Equation (5) implies a least-square solution

$$\mathbf{e} \approx (\Phi_{AIRS}^* \Phi_{AIRS})^{-1} \Phi_{AIRS}^* (\mathbf{F}_{AIRS} - \bar{\mathbf{F}}_{AIRS}) \quad (6)$$

where  $\Phi^*$  is the transpose of  $\Phi$ . Once  $\mathbf{e}$  is obtained, (4) can be used to derive the spectral fluxes at the channels sets (b)-(d). In practice, because of  $N_{AIRS} \gg M$ ,  $\Phi_{AIRS}$  is well-conditioned for every discrete intervals of  $(pw, \Delta T, T_s)$  and inversion of  $(\Phi_{AIRS}^* \Phi_{AIRS})$  is numerically stable.

In summary, this method finds the least-square-fit of the projections of AIRS-derived spectral fluxes onto the principal components. In practice, an AIRS channel could suffer from background electronic noise and, as a result, it might provide meaningful

observations most of the time but occasionally go wrong. This method is well suited for such situation since it only needs a subset of AIRS channels with valid calibrated radiances. Thus, it can tolerate a varying set of qualified channels from measurements to measurements. It makes use of information from all available good channels yet avoids the pains-taking error handling of bad channels for each individual measurement. A chart summarizing the whole algorithm described in section 3.1 and 3.2 is shown in Figure 4.

#### **4. Validation**

The validation of the whole algorithm described in section 3 is done in two folds. The first fold is “theoretical validation”—synthetic AIRS spectra are used to derive the spectral fluxes and the fluxes are compared with the ones directly computed from the MODTRAN5. The second fold is to use the algorithm to derive the broadband OLR from the AIRS spectrum and compare it with the collocated CERES OLR. The first one let us assess the whole algorithm without concerning the accuracy in spectroscopy and forward modeling since the MODTRAN5 is used as a surrogate of radiative transfer in the real world. The second one is more rigorous in the sense that all realistic uncertainties, such as those in spectroscopy, forward modeling, and collocation strategies, are taken into account.

##### **4.1 Theoretical validation**

ECWMF ERA-40 6-hourly temperature and humidity profiles between 60°S-60°N oceans in 1999 February (a different year and a different month from those ECWMF data

used in section 3) are randomly selected, classified to appropriate discrete intervals, and then the synthetic AIRS spectra at different zenith angles and LW spectral fluxes are computed from the MODTRAN5. For each discrete interval, about 400 random samples are archived. The differences between the spectral fluxes (or the broadband OLR) predicted from the synthetic AIRS spectra and the ones directly computed from the MODTRAN5 are examined. Figure 5 shows such differences for three different zenith angles,  $0^\circ$ ,  $21^\circ$ , and  $45^\circ$ . For all three angles, the mean differences for any discrete interval are generally within  $\pm 0.5 \text{ Wm}^{-2}$ . The standard deviations are no more than  $1.4 \text{ Wm}^{-2}$ . The maximum and minimum differences from individual comparisons are within  $\pm 5 \text{ Wm}^{-2}$ . The differences have no noticeable dependence on either the zenith angle or the discrete interval. The OLR differences for other zenith angles are consistent with what is shown in Figure 5.

Besides the difference in the broadband OLR, the differences between “predicted” and “directly computed” spectra fluxes are also examined. Figure 6 shows the mean differences in  $10 \text{ cm}^{-1}$  spectral fluxes for each discrete interval for  $21^\circ$  zenith angle. Noticeable compensating differences with opposite signs ( $\sim \pm 0.2$ - $0.5 \text{ Wm}^{-2}$ ,  $\pm 10$ - $18\%$  in fraction) exist in the water vapor rotation band, especially between  $400$ - $600 \text{ cm}^{-1}$ . For any  $10 \text{ cm}^{-1}$  interval in this spectral region, the sign of the difference is the same for all discrete intervals. These features indicate limitations of the multivariate regression scheme in estimating the  $10 \text{ cm}^{-1}$  spectral fluxes in the water vapor rotation band. Nevertheless, Figure 6 shows generally good agreement between the “predicted” spectral fluxes and the

“directly computed” spectral fluxes. As far as the spectral flux over a broader spectral range (e.g. the whole water vapor rotation band) is concerned, the difference would be even smaller due to the compensating differences from different portions of the broad range.

## 4.2 Comparison with collocated CERES observations

In order to test the performance of the algorithm, we collocate the AIRS spectra measured over the tropical oceans (30°S-30°N) in 2004 with the CERES cross-track clear-sky measurements, apply our algorithm to derive the broadband OLR, and then compare with the collocated CERES broadband OLR. In total, there are ~1.07 million qualified AIRS spectra and collocated CERES measurements for the whole year of 2004. The collocated measurements are further divided into two groups, one in ascending node and the other in descending node. For each group, the clear-sky OLR (OLR<sub>c</sub>) derived from AIRS spectra are averaged onto 2.5° longitude by 2° latitude grid boxes (the same grid boxes as used in the GFDL AM2 model) on a daily basis. So does the collocated CERES OLR<sub>c</sub>. Following comparisons are based on such daily-gridded OLR<sub>c</sub>.

Figure 7a shows the differences between the daily gridded clear-sky OLR derived from the AIRS descending-node spectra (OLR<sub>c</sub><sub>AIRS</sub>) and the counterparts from the CERES SSF product (OLR<sub>c</sub><sub>CERES</sub>). The mean difference averaged over all valid grid boxes within the tropics is ~ -0.1 Wm<sup>-2</sup> with little day-to-day variation. This is expected because the spectral ADMs are normalized with respect to corresponding CERES ADMs (refer to section 3.1 for the details). The standard deviation of OLR<sub>c</sub><sub>AIRS</sub>-OLR<sub>c</sub><sub>CERES</sub> is ~ 2.7 Wm<sup>-2</sup>, also with

little daily variation. For a single grid box in the area of interest, the maximum and minimum differences are no more than  $\pm 10 \text{ Wm}^{-2}$ , the minimum difference exhibiting a larger day-to-day fluctuation than the maximum difference. For the ascending node (Figure 7b), the mean difference is slightly above zero instead of slightly negative and other features are highly consistent with those in Figure 7a.

Based on the comparisons in subsection 4.1 and 4.2, it can be concluded that the algorithm is robust in estimating the broadband OLR and, to a large extent, it can obtain the spectral fluxes at  $10 \text{ cm}^{-1}$  or even larger intervals for the whole IR region with confidence.

## **5. Application in model evaluation — a case study with the GFDL AM2 simulation**

To illustrate the application of the derived spectral fluxes in GCM evaluation, we compare them with counterparts from the AM2 model simulation over the same period as forced by observed SST. As mentioned in section 2, the output of AM2 simulation is further sampled to ensure consistent temporal and spatial sampling patterns with the observations. All comparisons are based on such sub-sampled AM2 dataset. For simplicity, all comparisons are done with data collected during the ascending node only. Similar conclusions can be reached when the descending data is used in comparisons. Occasionally, in order to contrast the differences between model and observations, 2004 NCEP-DOE reanalysis data [Kanamitsu, *et al.*, 2002] is used to generate a “third-party” comparison. The 6-hourly NCEP-DOE reanalysis data is processed in the same way as the AM2 model output and corresponding synthetic spectral fluxes are computed from the

MODTRAN5. Section 5.1 focuses on the band-by-band IR fluxes directly output from the AM2. Section 5.2 discusses the comparison at a finer spectral resolution: the spectral fluxes over per  $10\text{cm}^{-1}$  intervals.

### 5.1 Band-by-band IR fluxes

AM2 LW radiation parameterization scheme output the LW fluxes over eight different spectral ranges (bands) as listed in Table 2. In practice, two of them ( $0\text{-}560\text{cm}^{-1}$ ,  $1400\text{-}2200\text{cm}^{-1}$ ) are treated together as a combined band. The absolute flux can vary by a factor of 2~8 from one spectral range to another spectral range. To make a better comparison across all spectral ranges, we focus on the clear-sky spectral greenhouse parameters [Ackerman, et al., 1992; Frey, et al., 1996] as well as the clear-sky broadband greenhouse parameters [Raval and Ramanathan, 1989] rather than the absolute clear-sky spectral fluxes over individual bands. The spectral greenhouse parameter is defined as

$$g_{\Delta\nu} = \frac{\int_{\Delta\nu} B_{\nu}(T_s) d\nu - F_{\Delta\nu}}{\int_{\Delta\nu} B_{\nu}(T_s) d\nu} \quad (6)$$

Where  $T_s$  is the surface temperature,  $\Delta\nu$  denotes the spectral range,  $B_{\nu}(T_s)$  is the blackbody radiation at frequency  $\nu$  and temperature  $T_s$ , and  $F_{\Delta\nu}$  is the clear-sky TOA outgoing flux over the same spectral range  $\Delta\nu$ . The spectral greenhouse parameter,  $g_{\Delta\nu}$ , is a measure of radiant energy over  $\Delta\nu$  trapped in the atmosphere:  $g_{\Delta\nu}=0$  when the atmosphere is transparent over  $\Delta\nu$  and  $g_{\Delta\nu}\rightarrow 1$  when atmosphere is opaque over  $\Delta\nu$  and emits to space at a temperature much colder than the surface temperature. When  $\Delta\nu$  spans over the whole LW region,  $g_{\Delta\nu}$  becomes the broadband greenhouse parameter (hereafter,  $g_{LW}$ ),

representing the fraction of total radiant energy left the surface but trapped in the atmosphere.

Figure 8a shows the 2004 annual-mean clear-sky broadband greenhouse parameter derived from the AM2 simulation. Intertropical Convergence Zone (ITCZ) and Southern Pacific Convergence Zone (SPCZ) are clearly associated with the maxima of clear-sky  $g_{\text{LW}}$  ( $\sim 0.43$ - $0.45$ ) because the two convergence zones tend to have higher humidity through the whole troposphere than the rest areas. Meanwhile, the large-scale subsidence drying tends to decrease the humidity in the middle and upper troposphere while the entrainment of marine stratus tends to dry the lower-tropospheric layer just above its top [Houze, 1993]. Thus the minima of clear-sky  $g_{\text{LW}}$  ( $\sim 0.30$ ) can be seen off the west coasts of continents where the marine stratus prevails and large-scale subsidence is prominent. The differences in the clear-sky  $g_{\text{LW}}$  between the AM2 and AIRS (Figure 8b) indicates that the AM2 overestimates  $g_{\text{LW}}$  over most of the tropical oceans and such overestimation, in general, is positively correlated with the  $g_{\text{LW}}$  itself. In the ITCZ and SPCZ, the overestimation could be as large as  $0.035$ - $0.04$  ( $\sim 7.8$ - $8.9\%$ ). Underestimations of  $g_{\text{LW}}$  by the AM2 happen in the subtropical oceans west of major continents and the central and eastern Pacific ( $90$ - $180^\circ\text{W}$ ) in the deep tropics, regions featured with large-scale subsidence. As we shall see later, such overestimations and underestimations in the broadband  $g_{\text{LW}}$  are in fact originated from different spectral ranges.

Figure 8c shows the simulated annual-mean clear-sky spectral greenhouse parameters (hereafter,  $g_{\Delta\nu}$ ) over the combined band of  $0$ - $560\text{cm}^{-1}$  and  $1400$ - $2200\text{cm}^{-1}$

(hereafter, the combined water vapor band). Both  $0\text{-}560\text{cm}^{-1}$  and  $1400\text{-}2200\text{cm}^{-1}$  bands are sensitive to relative humidity over a broad vertical layer from 600hPa to 200hPa. As a result, the  $g_{\Delta v}$  is highly correlated with water vapor amount in the middle and upper troposphere, with maxima over the ITCZ and SPCZ and minima over the large-scale subsidence regions. The corresponding AM2-AIRS difference shown in Figure 8d is positive over the whole tropical oceans. This suggests that the AM2 overestimates the relative humidity in the middle and upper troposphere. When a spectral range ( $900\text{-}990\text{ cm}^{-1}$ ) in the atmospheric window region is examined (Figure 8e), the  $g_{\Delta v}$  is much smaller than both the  $g_{\text{LW}}$  and the  $g_{\Delta v}$  of the combined water vapor band: the AM2-simulated  $g_{\Delta v}$  is only  $\sim 0.12\text{-}0.15$  in the ITCZ and SPCZ and  $\sim 0.04$  in the rest tropical oceans. This is because the atmosphere is almost transparent in the window region except the water vapor continuum absorption. The water vapor continuum absorption in this spectral region is proportional to the square of water vapor concentration, which means it is most sensitive to the water vapor concentration from surface to  $\sim 3\text{km}$ . The AM2-AIRS difference over this spectral range (Figure 8f) indicates an overestimation of  $\sim 0.02\text{-}0.04$  in the large-scale convergence zones. In the large-scale subsidence regions, especially the ocean west of major continents,  $g_{\Delta v}$  is underestimated by  $\sim 0.01\text{-}0.02$ . Same geographical patterns of the AM2-AIRS differences can be seen in other window regions as well ( $800\text{-}900\text{cm}^{-1}$ ,  $1070\text{-}1200\text{ cm}^{-1}$ , not shown here). Such differences suggest an overestimation of the lower tropospheric ( $0\text{-}3\text{km}$ ) humidity in the large-scale convergence zones and an underestimation of it in the large-scale subsidence regions by the AM2. At the large-scale



subsidence regions, the underestimation over the window regions (e.g. Figure 8f) slightly outplays the overestimation over the combined water vapor bands (Figure 8d) and other spectral ranges. As a result, the AM2 broadband  $g_{\text{LW}}$  at these regions are slightly underestimated. For the large-scale convergence zones, overestimations exist in all bands, together which leads to a  $\sim 10\%$  overestimation in the AM2 broadband  $g_{\text{LW}}$ .

Figure 8g shows the simulated  $g_{\Delta\nu}$  for the spectral range of  $990\text{-}1070\text{ cm}^{-1}$  (the ozone band). Unlike other spectral ranges discussed above, the simulated  $g_{\Delta\nu}$  of this spectral range has maxima in the subtropics rather than in the deep tropics, because of the higher lower stratospheric ozone concentrations in the subtropics than in the deep tropics. The AM2-AIRS differences (Figure 8h) show a zonally uniform pattern with minima in the deep tropics. Given the AM2 simulation is done with the 1990's ozone climatology, the AM2-AIRS differences here reflect (1) the difference of ozone distribution between the 1990's climatology used in the simulation and the actually ozone distribution in 2004, and (2) the lower stratospheric temperature difference between the AM2 simulation and the reality.

## 5.2 Comparisons of $10\text{cm}^{-1}$ spectral fluxes

When comparisons are conducted in finer spectral resolution than the eight spectral ranges in section 5.1, further compensating differences within a given band can be revealed. Figure 9a shows the annual-mean clear-sky spectral fluxes averaged over the whole tropical oceans for every  $10\text{cm}^{-1}$  intervals from  $10\text{-}2000\text{ cm}^{-1}$  as computed from the MODTRAN5 based on the AM2 output (the solid line) and as derived from collocated

AIRS and CERES observations (the dash line). The corresponding AM2-AIRS difference is shown in Figure 9c. The annual-mean spectral greenhouse parameters over the same  $10\text{cm}^{-1}$  spectral intervals are shown in Figure 9b and the corresponding AM2-AIRS difference in Figure 9d. The spectral flux difference from 10 to  $380\text{cm}^{-1}$  is in fact systematically positive, which is offset by relatively large negative difference in  $380\text{-}560\text{cm}^{-1}$  and leads to a negative difference in total for the spectral range of  $0\text{-}560\text{cm}^{-1}$ . Correspondingly, the AM2-AIRS difference in  $g_{\Delta\nu}$  is negative from 10 to  $380\text{cm}^{-1}$  and positive in  $380\text{-}560\text{cm}^{-1}$ , leading to a net positive difference for the  $0\text{-}560\text{cm}^{-1}$  band. The water vapor  $\nu_2$  band ( $\sim 1200\text{-}2000\text{cm}^{-1}$ ) has the highest  $g_{\Delta\nu}$  among all spectral ranges. It also contains compensating differences. For the  $\text{CO}_2$   $667\text{cm}^{-1}$  band, the flux ( $g_{\Delta\nu}$ ) differences in the band center are positive (negative) while those in the band wings are negative (positive), which indicating that the biases in the AM2-simulated tropospheric and stratospheric temperature have opposite signs.

Besides the annual mean  $g_{\Delta\nu}$ , monthly deviations (monthly anomalies) from the annual mean can be examined to reveal how the  $g_{\Delta\nu}$  at difference frequencies changes with seasons. Such monthly anomalies are shown in Figure 10a and 10b for the AM2 and observations, respectively. For the window regions, both the AM2 and observations show positive anomalies from January to June with maxima in April and negative anomalies in the rest months with minima in August. For part of the water vapor rotational bands ( $300\text{-}560\text{cm}^{-1}$ ) and the whole water vapor  $\nu_2$  band, both the AM2 and observations have maximum positive anomalies in April. However, the observed negative anomalies over the

same spectral regions peak in August while the simulated ones tend to have negative minima extend from August to October and even to December. For comparison, 6-hourly 2004 NCEP-DOE reanalysis [*Kanamitsu, et al.*, 2002] (NCEP-II) data is processed in the same way as the AM2 model output and the corresponding monthly anomalies of  $g_{\Delta\nu}$  is shown in Figure 10c. For NCEP-II reanalysis, the negative minima in the water vapor bands are concentrated in October, different from both the AM2 simulation and the AIRS-inferred observations. This reflects differences in simulated, assimilated, and observed seasonality of tropical middle and upper troposphere relative humidity, especially in the second half year. From 10 to  $300\text{cm}^{-1}$ , the AM2 and NCEP-II have positive maxima in April while the AIRS-inferred anomalies have moderate maxima in October. Given the uncertainties in our procedures of deriving  $g_{\Delta\nu}$  from the AIRS observations, the observed October maxima in Figure 10b might not be realistic. Both the AM2 and the observations reveal prominent seasonal variations of  $g_{\Delta\nu}$  around the  $\text{CO}_2$  band center ( $640\text{-}690\text{ cm}^{-1}$ ) but the peaks in the AM2 lag those in the observations by 1-2 months, suggesting the discrepancies in simulating the phase of seasonal variations in the middle and lower stratospheric temperature. NCEP-II, on the other hand, agrees with the observations to a large extent for both the phase and amplitude of the seasonal variations in the  $\text{CO}_2$  band center. The observations exhibit a strong seasonal variation in the  $\text{O}_3$  band center ( $1010\text{-}1065\text{ cm}^{-1}$ ) with maximum in July-September and minimum in January-March. This seasonal variation is primarily due to the seasonal changes of ozone concentration because, when a constant tropical-mean ozone profile is used in the

MODTRAN5 for generating all synthetic spectral fluxes for both the AM2 and NCEP-II, such seasonal variations in the ozone band is hardly seen (Figure 11a and 11c).

Subsection 5.1 and 5.2 demonstrates that the spectral fluxes derived from the collocated AIRS and CERES data can be used to evaluate climate models in various ways. The band-by-band fluxes calculated in the GCM can be directly compared with the derived spectral fluxes. Compensating errors among different bands can be disclosed in this way. Also, using a narrow-band radiative transfer model like the MODTRAN5, comparison could be done at even finer spectral resolution and compensating errors within an individual band can be reveals. The dense sampling pattern of AIRS and CERES and re-sampling of GCM output according to the satellite track ensure meaningful comparisons of the spatial distributions and temporal evolutions of such spectral fluxes.

## **6. Conclusions and discussions**

Collocated AIRS and CERES observations are used in this study to derive clear-sky outgoing spectral flux at  $10\text{cm}^{-1}$  interval from 10 to  $2000\text{cm}^{-1}$ . The spectral ADMs are developed based on the CERES scene types and the corresponding CERES SSF broadband ADMs. Such ADMs are then used to convert the AIRS radiances to spectral fluxes. The fluxes at spectral regions not covered by the AIRS instrument are derived using a multivariate regression schemes. The whole algorithm is validated against synthetic spectra as well as the collocated CERES broadband OLR. The focus of this study is clear-sky observations over the tropical oceans. Yet the whole methodology is applicable to clear-sky scenes over other surface types since the validated CERES SSF

broadband ADMs for other surface types are also available [Loeb *et al.*, 2007].

Using the GFDL AM2 model as a case study, the applications of the derived clear-sky spectral fluxes in GCM evaluations are also discussed. Such spectral fluxes can reveal the compensating errors that cannot be detected in tradition comparison of the broadband OLR. Ccompensating errors from different broad spectral ranges as well as within a given spectral ranges can be quantitatively revealed. The comparisons with the AM2 simulation show how the spatial distribution and temporal evolution of water vapor at different part of the troposphere contribute to the spectral flux differences. As showed in Figure 8, the AM2 tends to be more humid than the observations in the middle and upper troposphere for the whole tropical oceans. In the lower troposphere, it tends to be more humid in the large-scale convergence zones but dryer in the large-scale subsidence zones. This suggests dynamical causes of simulated water vapor biases. As for the seasonal variations of the spectral fluxes in the water vapor rotational band and  $\nu_2$  band, model aggress with the AIRS observation and NCEP-II reanalysis for the first half year but not for the second half year: the AM2 model has large negative anomalies spanning from August to December while the observations show negative minima concentrated in August and the NCPE-II data has negative minima in October. Such discrepancies among model, observations, and reanalysis in the spectral domain confirm the value of infrared spectral fluxes in model evaluation. The influences of ozone spatial distributions and temporal evolutions can also be seen from the comparisons.

This study serves as the first step toward deriving the TOA spectral cloud radiative

forcing. Like the simulated broadband OLR, the simulated broadband cloud radiative forcing could be right for the wrong reasons because of the compensating errors originated from different spectral ranges. The similar methodology established in this study can be extended to the collocated AIRS and CERES cloudy observations so the TOA all-sky spectral fluxes can be derived. Then the TOA spectral cloud radiative forcing can be derived by differencing the TOA clear-sky and all-sky spectral fluxes. The clear-sky spectral fluxes and the spectral cloud radiative forcing consist of a suite of more stringent test for GCM than the broadband counterparts because, to a large extent, they resolve the compensating biases from different spectral ranges. For a GCM agreeing with observations in both the clear-sky spectral fluxes and the spectral cloud radiative forcing, there would be more confidences in its representations of the underlying physical processes, and thus more confidences in the climate predictions made by it.

The confidence in the spectral fluxes derived from the collocated AIRS and CERES observations depends on the accuracy of the algorithm described in section 3. Errors in the derived spectral fluxes could originate from various sources. The mean spectral fluxes and the corresponding principal components used in the multivariate regression schemes have their limitations since they are derived from a set of finite samples. Another source of error exists in the forward radiative transfer modeling, MODTRAN5, especially in the far IR, a spectral range not covered by the AIRS instrument and therefore purely relying on the MODTRAN5 and the regression scheme. The importance of far-IR water vapor absorption to the clear-sky radiative budget has been long recognized [*Clough, et al., 1992*;

*Sinha and Harries*, 1995; 1997]. This study has to infer the far-IR spectral fluxes since AIRS has no coverage in the far IR. Such inferences is feasible because of the redundant information content between the water vapor rotation band and the water vapor  $\nu_2$  band, the latter being largely covered by the AIRS instrument. To a large extent, the regression scheme infers the far-IR spectra fluxes via the close correlations between the two water vapor bands. With more efforts investigated on directly observing spectrally-resolve radiance in the far IR from space [*Mlynchak, et al.*, 2006; *Palchetti, et al.*, 2006], this situation could be improved in the future by merging observations from multiple spectrometer instruments to create a merged dataset of spectral fluxes over the whole IR.

### **Acknowledgements**

The AIRS data were obtained from NASA GSFC DAAC and the CERES data from NASA Langley DAAC. The NCEP-DOS reanalysis data were obtained from <http://www.cdc.noaa.gov>. The ECMWF reanalysis data were obtained from [http://data.ecmwf.int/data/d/era40\\_daily/](http://data.ecmwf.int/data/d/era40_daily/). We thank R. Hemler, Y. Huang, L. Strow, L. Chen, E. Fishbein for valuable discussions and helps. One of the authors, Wenze yang, was supported by a University of Michigan internal fund.

## References

- Ackerman, S. A., et al. (1992), Radiation Budget Studies Using Collocated Observations from Advanced Very High-Resolution Radiometer, High-Resolution Infrared Sounder/2, and Earth Radiation Budget Experiment Instruments, *J. Geophys. Res.-Atmos.*, *97*, 11513-11525.
- Allan, R. P., et al. (2004), Simulation of the Earth's radiation budget by the European centre for Medium-Range Weather Forecasts 40-year reanalysis (ERA40), *J. Geophys. Res.-Atmos.*, *109*, D18107, doi:10.1029/2004JD004816.
- Anderson, G., et al. (2006), Atmospheric Sensitivity to Spectral Top-of-Atmosphere Solar Irradiance Perturbations, Using MODTRAN-5 Radiative Transfer Algorithm, *EOS Trans. AGU*, *87*(52), Fall Meet. Suppl., Abstract A11C-05, 2006.
- Aumann, H. H., et al. (2003), AIRS/AMSU/HSB on the aqua mission: Design, science objectives, data products, and processing systems, *IEEE Trans. Geosci. Remote Sens.*, *41*, 253-264.
- Barkstrom, B. R. (1984), The Earth Radiation Budget Experiment (ERBE), *Bull. Am. Meteorol. Soc.*, *65*, 1170-1185.
- Berk, A., et al. (1998), MODTRAN cloud and multiple scattering upgrades with application to AVIRIS, *Remote Sens. Environ.*, *65*, 367-375.
- Bernstein, L. S., et al. (1996), Very narrow band model calculations of atmospheric fluxes and cooling rates, *J. Atmos. Sci.*, *53*, 2887-2904.
- Chahine, M. T., et al. (2006), AIRS: Improving weather forecasting and providing new



data on greenhouse gases, *Bull. Am. Meteorol. Soc.*, 87, 911-926.

Clough, S. A., and M. J. Iacono (1995), Line-by-Line Calculation of Atmospheric Fluxes and Cooling Rates .2. Application to Carbon-Dioxide, Ozone, Methane, Nitrous-Oxide and the Halocarbons, *J. Geophys. Res.-Atmos.*, 100, 16519-16535.

Clough, S. A., et al. (1992), Line-by-Line Calculations of Atmospheric Fluxes and Cooling Rates - Application to Water-Vapor, *J. Geophys. Res.-Atmos.*, 97, 15761-15785.

Clough, S. A., et al. (2005), Atmospheric radiative transfer modeling: a summary of the AER codes, *J. Quant. Spectrosc. Radiat. Transfer*, 91, 233-244.

Feldman, D. R., et al. (2006), Direct retrieval of stratospheric CO<sub>2</sub> infrared cooling rate profiles from AIRS data, *Geophys. Res. Lett.*, 33, L11803, doi:10.1029/2005GL024680.

Frey, R. A., et al. (1996), Climate parameters from satellite spectral measurements .1. Collocated AVHRR and HIRS/2 observations of spectral greenhouse parameter, *J. Clim.*, 9, 327-344.

Gaiser, S. L., et al. (2003), In-flight spectral calibration of the atmospheric infrared sounder, *IEEE Trans. Geosci. Remote Sens.*, 41, 287-297.

Goodberlet, M. A., et al. (1990), Ocean Surface Wind-Speed Measurements of the Special Sensor Microwave Imager (SSM/I), *IEEE Trans. Geosci. Remote Sens.*, 28, 823-828.

Harries, J. E., et al. (2005), The Geostationary Earth Radiation Budget (GERB) Project, *Bull. Am. Meteorol. Soc.*, 86, 945-960.

Haskins, R., et al. (1999), Radiance covariance and climate models, *J. Clim.*, 12, 1409-1422.

Horowitz, L. W. (2006), Past, present, and future concentrations of tropospheric ozone and aerosols: Methodology, ozone evaluation, and sensitivity to aerosol wet removal, *J. Geophys. Res.-Atmos.*, *111*, D22211, doi:10.1029/2005JD006937.

Houze, R. A. (1993), *Cloud Dynamics*, 573pp., Elsevier, New York.

Huang, X. L., et al. (2003), Analysis of thermal emission spectrometer data using spectral EOF and tri-spectral methods, *Icarus*, *165*, 301-314.

Huang, X. L., and Y. L. Yung (2005), Spatial and spectral variability of the outgoing thermal IR spectra from AIRS: A case study of July 2003, *J. Geophys. Res.-Atmos.*, *110*, D12102, doi:10.1029/2004JD005530.

Kanamitsu, M., et al. (2002), NCEP-DOE AMIP-II reanalysis (R-2), *Bull. Am. Meteorol. Soc.*, *83*, 1631-1643.

Loeb, N. G., et al. (2005), Angular distribution models for top-of-atmosphere radiative flux estimation from the Clouds and the Earth's Radiant Energy System instrument on the Terra satellite. Part I: Methodology, *J. Atmos. Oceanic Technol.*, *22*, 338-351.

Loeb, N. G., et al. (2007), Angular distribution models for top-of-atmosphere radiative flux estimation from the Clouds and the Earth's Radiant Energy System instrument on the Terra satellite. Part II: Validation, *J. Atmos. Oceanic Technol.*, *24*, 564-584.

Loeb, N. G., et al. (2003), Angular distribution models for top-of-atmosphere radiative flux estimation from the clouds and the Earth's Radiant Energy System instrument on the Tropical Rainfall Measuring Mission satellite. part I: Methodology, *J. App. Meteorol.*, *42*, 240-265.

- Mlynczak, M. G., et al. (2006), First light from the Far-Infrared Spectroscopy of the Troposphere (FIRST) instrument, *Geophys. Res. Lett.*, *33*, L07704, doi:10.1029/2005GL025114.
- Pagano, T. S., et al. (2003), Prelaunch and in-flight radiometric calibration of the Atmospheric Infrared Sounder (AIRS), *IEEE Trans. Geosci. Remote Sens.*, *41*, 265-273.
- Palchetti, L., et al. (2006), Technical note: First spectral measurement of the Earth's upwelling emission using an uncooled wideband Fourier transform spectrometer, *Atmos. Chem. Phys.*, *6*, 5025-5030.
- Parkinson, C. L. (2003), Aqua: An earth-observing satellite mission to examine water and other climate variables, *IEEE Trans. Geosci. Remote Sens.*, *41*, 173-183.
- Ramanathan, V., et al. (1989), Cloud-Radiative Forcing and Climate - Results from the Earth Radiation Budget Experiment, *Science*, *243*, 57-63.
- Randel, W. J., and F. Wu (2007), A stratospheric ozone profile data set for 1979-2005: Variability, trends, and comparisons with column ozone data, *J. Geophys. Res.-Atmos.*, *112*, D06313, 10.1029/2006JD007339.
- Raval, A., et al. (1994), Observed Dependence of Outgoing Longwave Radiation on Sea-Surface Temperature and Moisture, *J. Clim.*, *7*, 807-821.
- Raval, A., and V. Ramanathan (1989), Observational Determination of the Greenhouse-Effect, *Nature*, *342*, 758-761.
- Rothman, L. S., et al. (2005), The HITRAN 2004 molecular spectroscopic database, *J. Quant. Spectrosc. Radiat. Transfer*, *96*, 139-204.

- Rothman, L. S., et al. (1998), The HITRAN molecular spectroscopic database and HAWKS (HITRAN Atmospheric Workstation): 1996 edition, *J. Quant. Spectrosc. Radiat. Transfer*, *60*, 665-710.
- Sinha, A., and J. E. Harries (1995), Water-Vapor and Greenhouse Trapping - the Role of Far-Infrared Absorption, *Geophys. Res. Lett.*, *22*, 2147-2150.
- Sinha, A., and J. E. Harries (1997), The earth's clear-sky radiation budget and water vapor absorption in the far infrared, *J. Clim.*, *10*, 1601-1614.
- Slingo, A., et al. (1998), A 15-year simulation of the clear-sky greenhouse effect using the ECMWF reanalyses: Fluxes and comparisons with ERBE, *J. Clim.*, *11*, 690-708.
- Slingo, A., and M. J. Webb (1992), Simulation of Clear-Sky Outgoing Longwave Radiation over the Oceans Using Operational Analyses, *Quar. J. Roy. Meteorol. Soc.*, *118*, 1117-1144.
- Strow, L. L., et al. (2006), Validation of the Atmospheric Infrared Sounder radiative transfer algorithm, *J. Geophys. Res.-Atmos.*, *111*, D09S06, doi:10.1029/2005JD006146.
- Strow, L. L., et al. (2003), Prelaunch spectral calibration of the Atmospheric Infrared Sounder (AIRS), *IEEE Trans. Geosci. Remote Sens.*, *41*, 274-286.
- Uppala, S. M., et al. (2005), The ERA-40 re-analysis, *Quart. J. Roy. Meteorol. Soc.*, *131*, 2961-3012.
- Wielicki, B. A., et al. (1996), Clouds and the earth's radiant energy system (CERES): An earth observing system experiment, *Bull. Am. Meteorol. Soc.*, *77*, 853-868.
- Wielicki, B. A., et al. (2002), Evidence for large decadal variability in the tropical mean

radiative energy budget, *Science*, 295, 841-844.

Yang, S. K., et al. (1999), Evaluation of the earth radiation budget in NCEP-NCAR reanalysis with ERBE, *J. Clim.*, 12, 477-493.

Table 1. The 14 discrete intervals of precipitable water ( $pw$ ), lapse rate ( $\Delta T$ ) that is defined as the vertical temperature change of the first 300hPa above the surface, and surface skin temperature ( $T_s$ ) used in the CERES LW ADMs to determine clear-sky OLR over the oceans.

Discrete interval	$pw(\text{cm})$	$\Delta T(\text{K})$	$T_s (\text{K})$
1	0-1	<15	270-290
2	0-1	<15	290-310
3	0-1	15-30	270-290
4	0-1	15-30	290-310
5	1-3	<15	270-290
6	1-3	<15	290-310
7	1-3	15-30	270-290
8	1-3	15-30	290-310
9	1-3	15-30	310-330
10	3-5	<15	270-290
11	3-5	<15	290-310
12	3-5	15-30	290-310
13	>5	<15	290-310
14	>5	15-30	290-310

Table 2. List of eight spectral ranges at which the AM2 LW parameterization schemes directly output the TOA band-by-band fluxes

	Spectral Range (cm <sup>-1</sup> )	Primary absorbers
1*	0-560	H <sub>2</sub> O
2	560-800	CO <sub>2</sub> , N <sub>2</sub> O
3	800-900	H <sub>2</sub> O continuum
4	900-990	H <sub>2</sub> O continuum
5	990-1070	O <sub>3</sub>
6	1070-1200	H <sub>2</sub> O continuum
7	1200-1400	H <sub>2</sub> O, CH <sub>4</sub> , N <sub>2</sub> O
8*	1400-2200	H <sub>2</sub> O

\* In practice, spectral range 1 and 8 are treated together as a combined band and the model output the TOA flux of the combined band.

## Figure Captions

Figure 1. The surface footprints of AIRS (solid gray circles) and CERES (open black circles) as observed from about 01:06:15 to 01:06:45 UTC on January 1, 2005.

Figure 2. a) The spectrally-dependent anisotropic factors based on the US 1976 standard atmosphere profile. The Solid gray line is for  $0^\circ$  zenith angle and the black dash line is for  $60^\circ$  zenith angle. The upwelling flux is the top-of-atmosphere (TOA) flux. b) Same as a) except that the upwelling flux is the flux at 9km above the surface.

Figure 3. The solid line with diamonds is LW broadband anisotropic factor used in the CERES SSF product for the daytime clear-sky scenes over the ocean with  $pw = 1-3$  cm,  $\Delta T < 15K$ , and  $T_s = 290-310K$  (discrete interval 6 in Table 1). The solid line with circles is used for the corresponding nighttime clear-sky scenes in the CERES SSF product. The thick dash line is the LW broadband anisotropic factor derived from the procedure described in section 3.1.

Figure 4. Flow-chart illustration of the algorithm described in section 3- the derivation of spectral flux over the whole IR region from the collocated AIRS and CERES measurements. Notations are the same as defined in the context (section 3).

Figure 5. (a) Difference between the OLR predicted from the synthetic nadir-view AIRS spectra ( $0^\circ$  zenith angle) and directly computed OLR from MODTRAN<sup>TM</sup>-5 for 14 discrete intervals of CERES clear-sky ADMs listed in Table 1. Approximately 400 profiles randomly selected from ECMWF datasets are used for each discrete interval. The diamond



is the mean difference, the error bar shows the mean $\pm$ standard deviation, the dash lines are the maximum and minimum differences for all random profiles in a given discrete interval.

(b) Same as (a) except the zenith angle of 21°. (c) Same as (a) except the zenith angle of 45°.

Figure 6. The mean difference between the predicted TOA spectra fluxes based on synthetic AIRS spectra and the directly computed TOA spectral fluxes from MODTRAN<sup>TM</sup>-5 for each discrete interval used in the ADM. The spectral flux is computed for every 10cm<sup>-1</sup> interval from 10-2000cm<sup>-1</sup>. Ordinate represents the 14 discrete intervals of CERES clear-sky ADMs listed in Table 1. Approximately 400 profiles randomly selected from ECMWF datasets are used to calculate the mean difference for each discrete interval. The unit of the mean difference is W per m<sup>2</sup> per 10cm<sup>-1</sup>.

Figure 7. (a) The daily difference between the clear-sky OLR (OLR<sub>c</sub>) over the tropical oceans estimated from AIRS spectra measured during descending node and that from the collocated CERES measurement. The temporal coverage is from January to December of 2004. Individual collocated observations are gridded onto 2.5°×2° grid boxes on a daily basis before the difference is taken. The black solid line is the averaged daily difference over all valid grid boxes. The black dash lines are the mean $\pm$ standard deviation. The gray dotted lines are the maximum and minimum differences for all validate grid boxes. (b) Same as (a) except for the ascending node.

Figure 8 (a) The 2004 annual-mean broadband greenhouse parameters ( $g_{LW}$ ) over the tropical oceans simulated by the AM2. (b) The difference between AM2-simulated and

AIRS-inferred  $g_{LW}$ . (c)-(d) Same as (a)-(b) except for the spectral greenhouse parameters over combined spectral ranges of  $0-560\text{cm}^{-1}$  and  $1400-2200\text{cm}^{-1}$ . (e)-(f) and (g)-(h), same as (c)-(d) except for spectral ranges of  $560-800\text{cm}^{-1}$  and  $990-1070\text{cm}^{-1}$ , respectively. Please note four different colorbars, corresponding to four different sets of value range, are used.

Figure 9. (a) The annual-mean clear-sky spectral flux (per  $10\text{cm}^{-1}$  intervals) over the tropical oceans as inferred from the AIRS and CERES collocated observations (dash line) and simulated from MODTRAN5 based on the AM2 6-hourly output (solid line). (b) Same as (a) except for annual-mean clear-sky spectral greenhouse parameters ( $g_{\Delta\nu}$ ) at  $10\text{cm}^{-1}$  intervals. The annual-mean  $g_{\Delta\nu}$  is derived from twelve monthly means of  $g_{\Delta\nu}$ . (c) The differences between the AM2-simulated and the AIRS-inferred spectra fluxes shown in (a). (d) The differences between the AM2 and AIRS  $g_{\Delta\nu}$  shown in (b).

Figure 10. (a) The AM2 monthly deviations (anomalies) of the clear-sky spectral greenhouse parameters  $g_{\Delta\nu}$  (per  $10\text{cm}^{-1}$  interval) from the annual mean  $g_{\Delta\nu}$  (the solid line in Figure 9b) as computed from MODTRAN<sup>TM</sup>-5. (b) Same as (a) except for the  $g_{\Delta\nu}$  derived from collocated AIRS and CERES observations. (c) Same as (a) except for the 2004 NCEP-DOE reanalysis 6-hourly output. The 6-hourly NCEP-DOE reanalysis is processed in a way similar to the AM2 output.

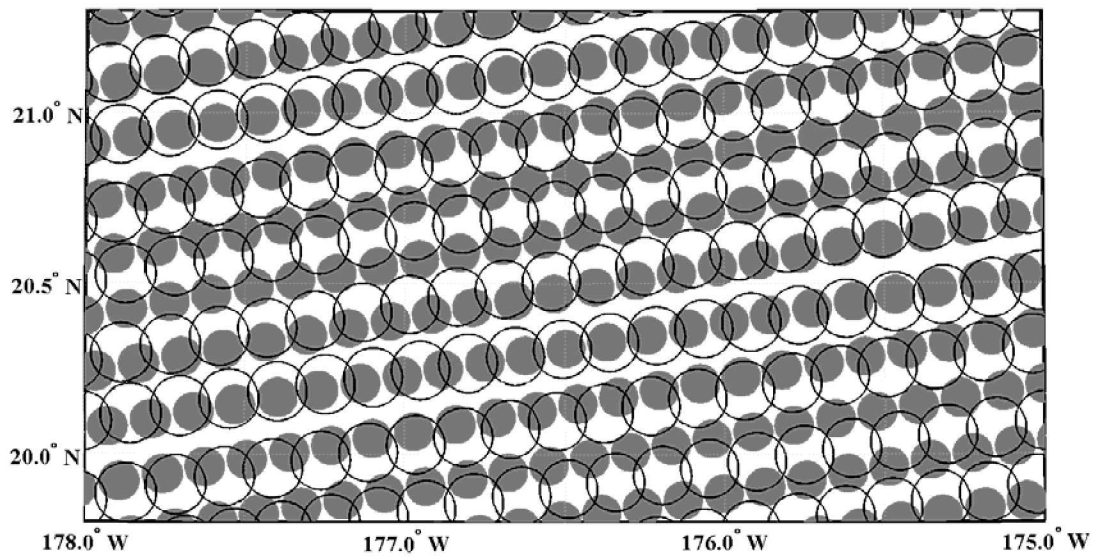


Figure 1. The surface footprints of AIRS (solid gray circles) and CERES (open black circles) as observed from about 01:06:15 to 01:06:45 UTC on January 1, 2005.

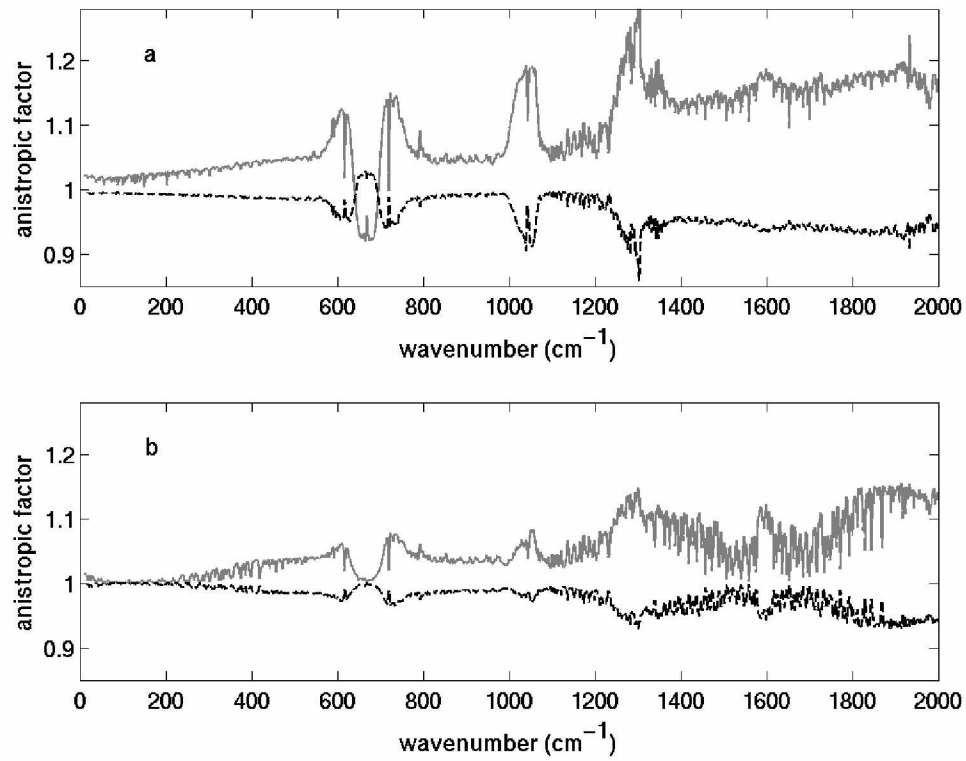


Figure 2. a) The spectrally-dependent anisotropic factors based on the US 1976 standard atmosphere profile. The solid gray line is for  $0^\circ$  zenith angle and the black dash line is for  $60^\circ$  zenith angle. The upwelling flux is the top-of-atmosphere (TOA) flux. b) Same as a) except that the upwelling flux is the flux at 9km above the surface.

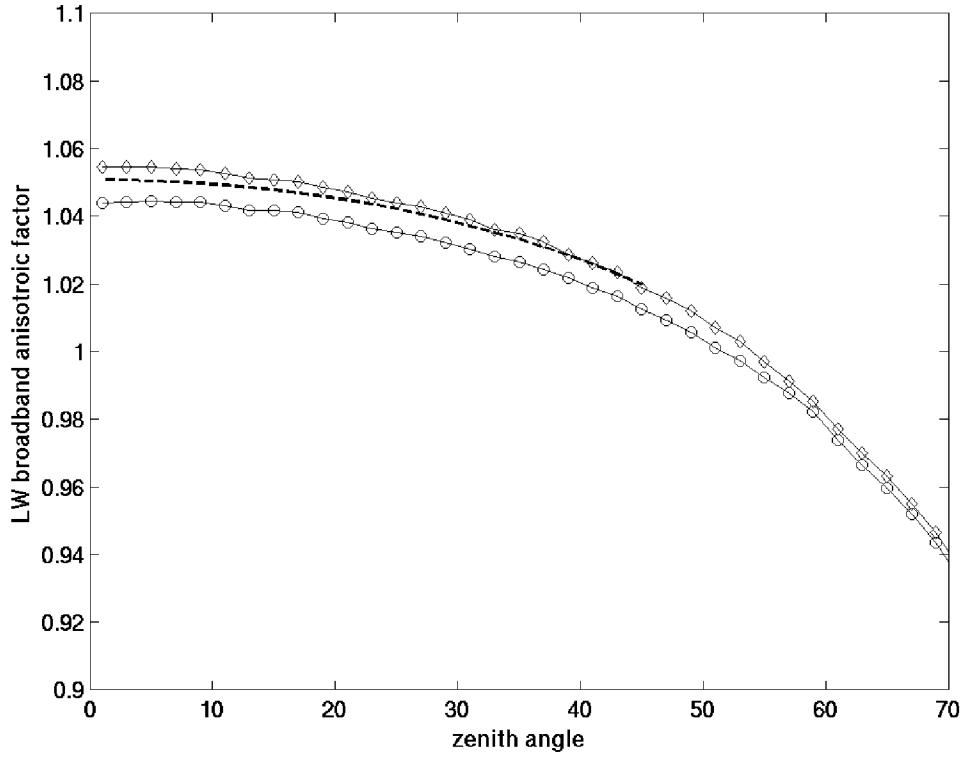


Figure 3. The solid line with diamonds is LW broadband anisotropic factor used in the CERES SSF product for the daytime clear-sky scenes over the ocean with  $pw = 1-3$  cm,  $\Delta T < 15K$ , and  $T_s = 290-310K$  (discrete interval 6 in Table 1). The solid line with circles is used for the corresponding nighttime clear-sky scenes in the CERES SSF product. The thick dash line is the LW broadband anisotropic factor derived from the procedure described in section 3.1.

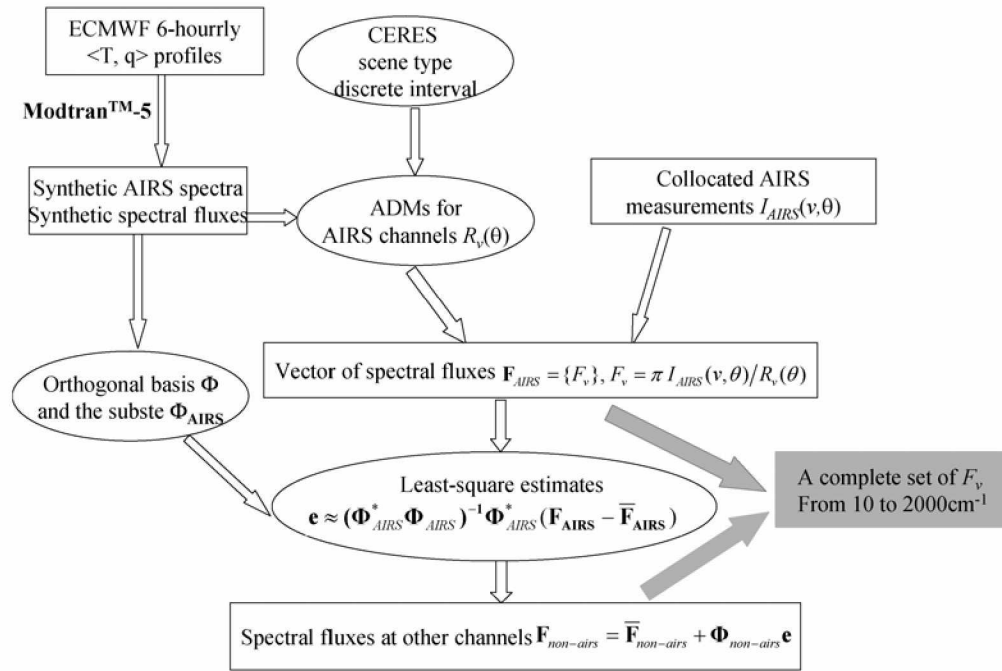


Figure 4. Flow-chart illustration of the algorithm described in section 3- the derivation of spectral flux over the whole IR region from the collocated AIRS and CERES measurements. Notations are the same as defined in the context (section 3).

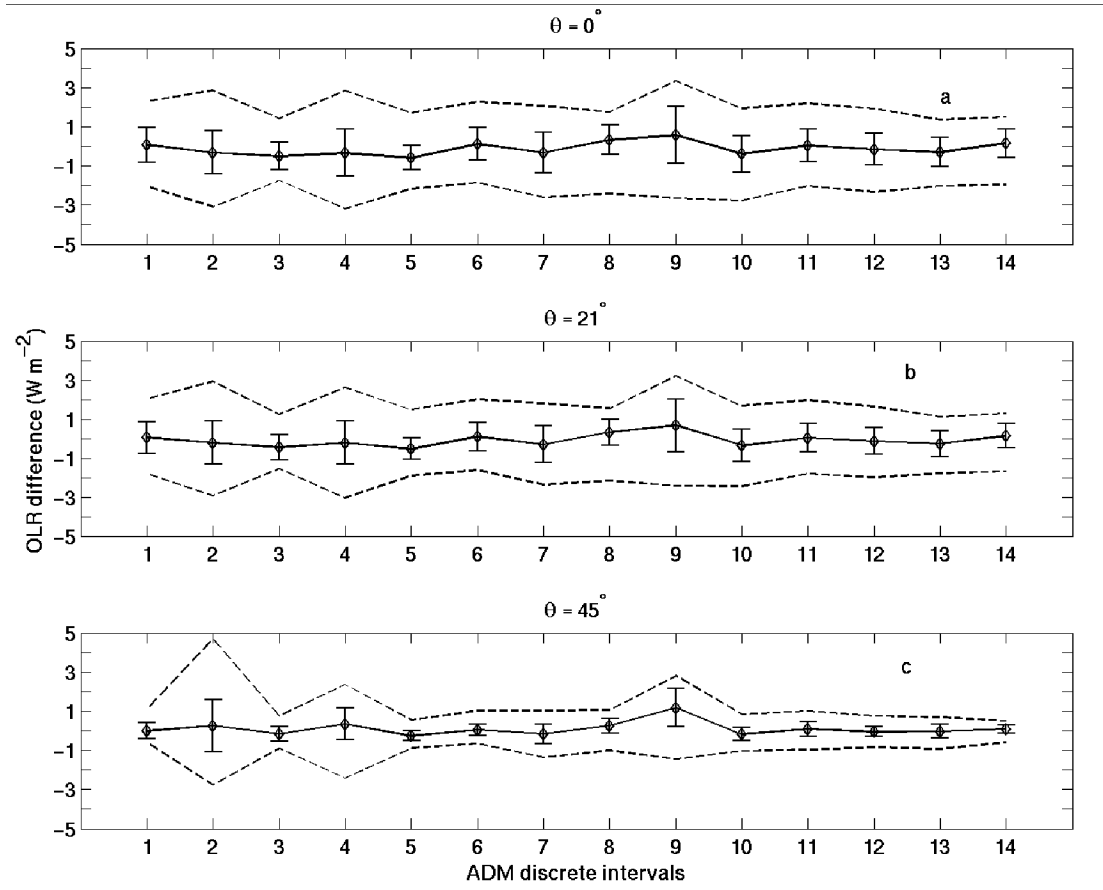


Figure 5. (a) Difference between the OLR predicted from the synthetic nadir-view AIRS spectra ( $0^\circ$  zenith angle) and directly computed OLR from MODTRAN™-5 for 14 discrete intervals of CERES clear-sky ADMs listed in Table 1. Approximately 400 profiles randomly selected from ECMWF datasets are used for each discrete interval. The diamond is the mean difference, the error bar shows the mean $\pm$ standard deviation, the dash lines are the maximum and minimum differences for all random profiles in a given discrete interval. (b) Same as (a) except the zenith angle of  $21^\circ$ . (c) Same as (a) except the zenith angle of  $45^\circ$ .

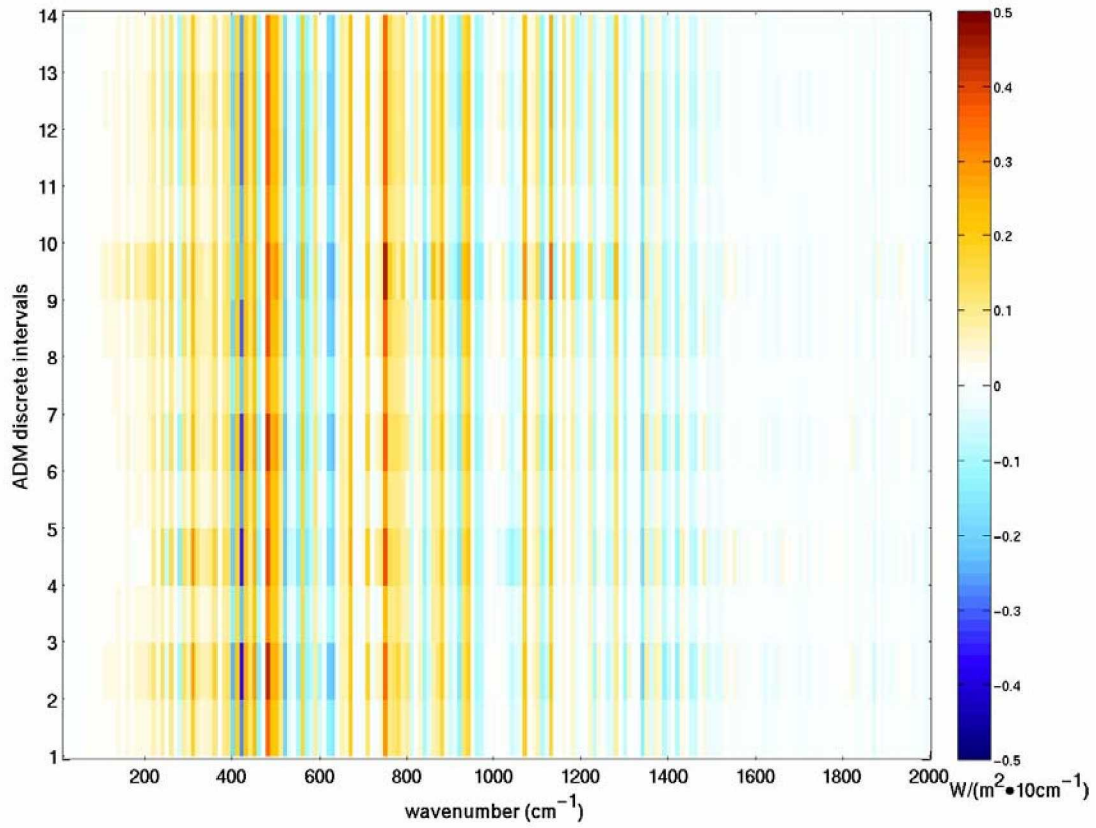


Figure 6. The mean difference between the predicted TOA spectra fluxes based on synthetic AIRS spectra and the directly computed TOA spectral fluxes from MODTRAN<sup>TM</sup>-5 for each discrete interval used in the ADM. The spectral flux is computed for every 10cm<sup>-1</sup> interval from 10-2000cm<sup>-1</sup>. Ordinate represents the 14 discrete intervals of CERES clear-sky ADMs listed in Table 1. Approximately 400 profiles randomly selected from ECMWF datasets are used to calculate the mean difference for each discrete interval. The unit of the mean difference is W per m<sup>2</sup> per 10cm<sup>-1</sup>.



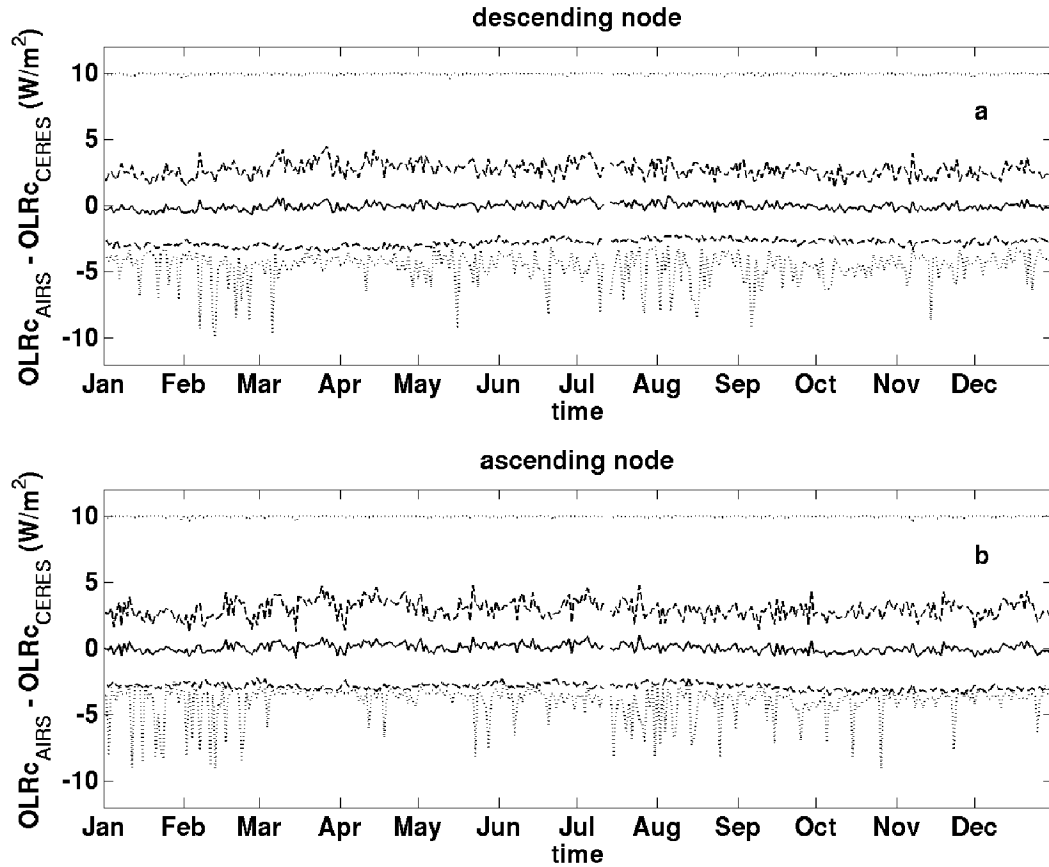


Figure 7. (a) The daily difference between the clear-sky OLR ( $OLRc$ ) over the tropical oceans estimated from AIRS spectra measured during descending node and that from the collocated CERES measurement. The temporal coverage is from January to December of 2004. Individual collocated observations are gridded onto  $2.5^\circ \times 2^\circ$  grid boxes on a daily basis before the difference is taken. The black solid line is the averaged daily difference over all valid grid boxes. The black dash lines are the mean  $\pm$  standard deviation. The gray dotted lines are the maximum and minimum differences for all validate grid boxes. (b) Same as (a) except for the ascending node.

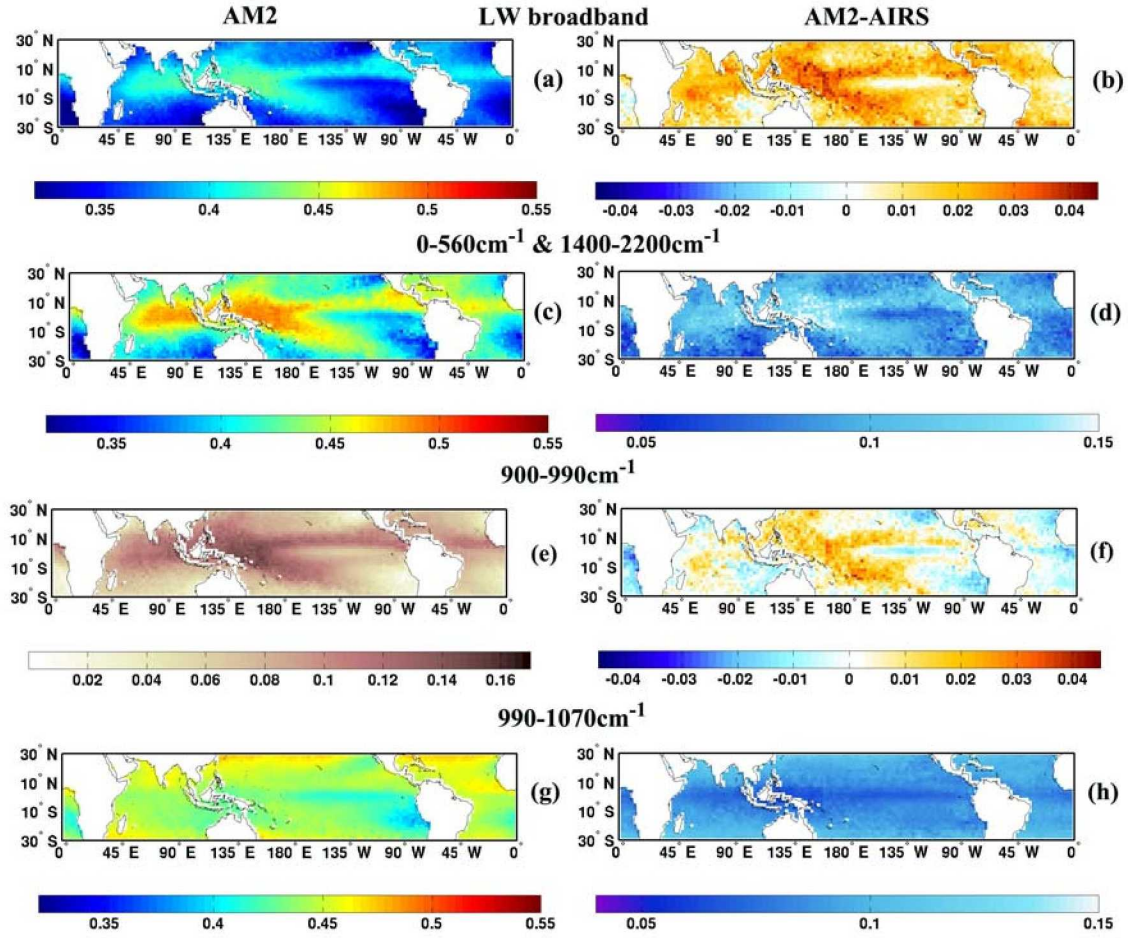


Figure 8. (a) The 2004 annual-mean broadband greenhouse parameters ( $g_{LW}$ ) over the tropical oceans simulated by the AM2. (b) The difference between AM2-simulated and AIRS-inferred  $g_{LW}$ . (c)-(d) Same as (a)-(b) except for the spectral greenhouse parameters over combined spectral ranges of 0-560cm<sup>-1</sup> and 1400-2200cm<sup>-1</sup>. (e)-(f) and (g)-(h), same as (c)-(d) except for spectral ranges of 560-800cm<sup>-1</sup> and 990-1070cm<sup>-1</sup>, respectively. Please note four different colorbars, corresponding to four different sets of value range, are used here.

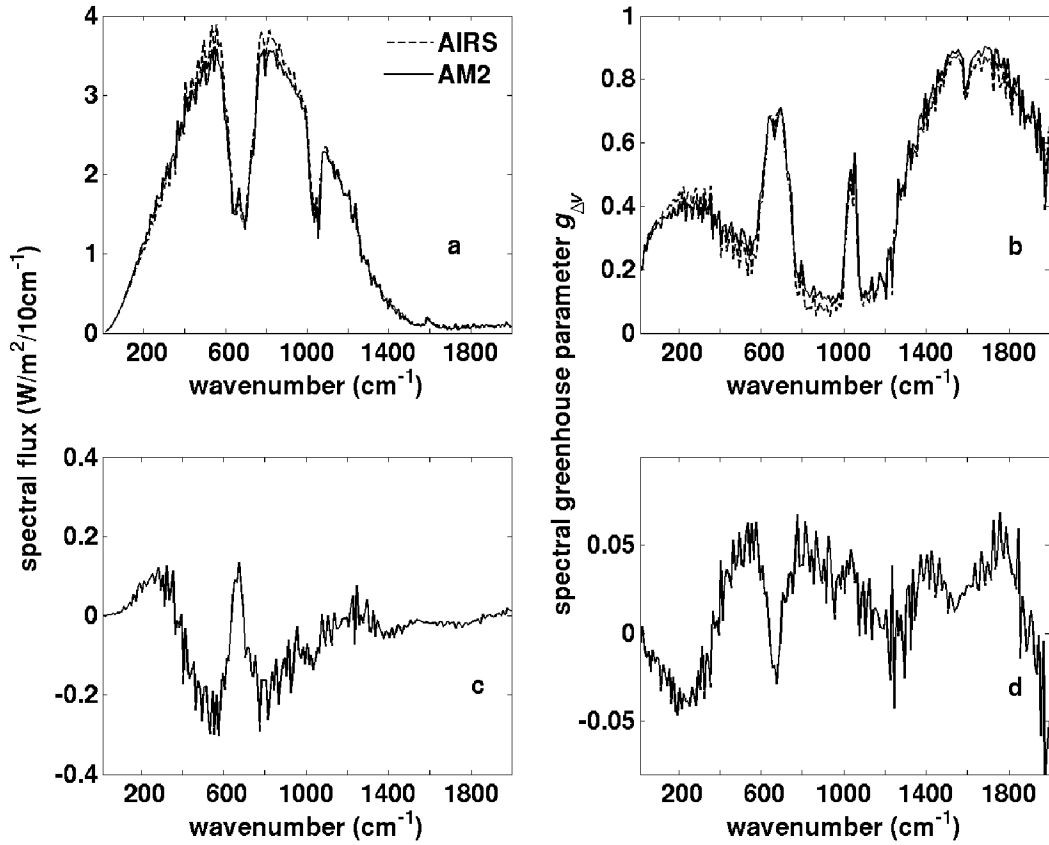


Figure 9. (a) The annual-mean clear-sky spectral flux (per 10cm<sup>-1</sup> intervals) over the tropical oceans as inferred from the AIRS and CERES collocated observations (dash line) and simulated from MODTRAN5 based on the AM2 6-hourly output (solid line). (b) Same as (a) except for annual-mean clear-sky spectral greenhouse parameters ( $g_{\Delta\nu}$ ) at 10cm<sup>-1</sup> intervals. The annual-mean  $g_{\Delta\nu}$  is derived from twelve monthly means of  $g_{\Delta\nu}$ . (c) The differences between the AM2-simulated and the AIRS-inferred spectra fluxes shown in (a). (d) The differences between the AM2 and AIRS  $g_{\Delta\nu}$  shown in (b).

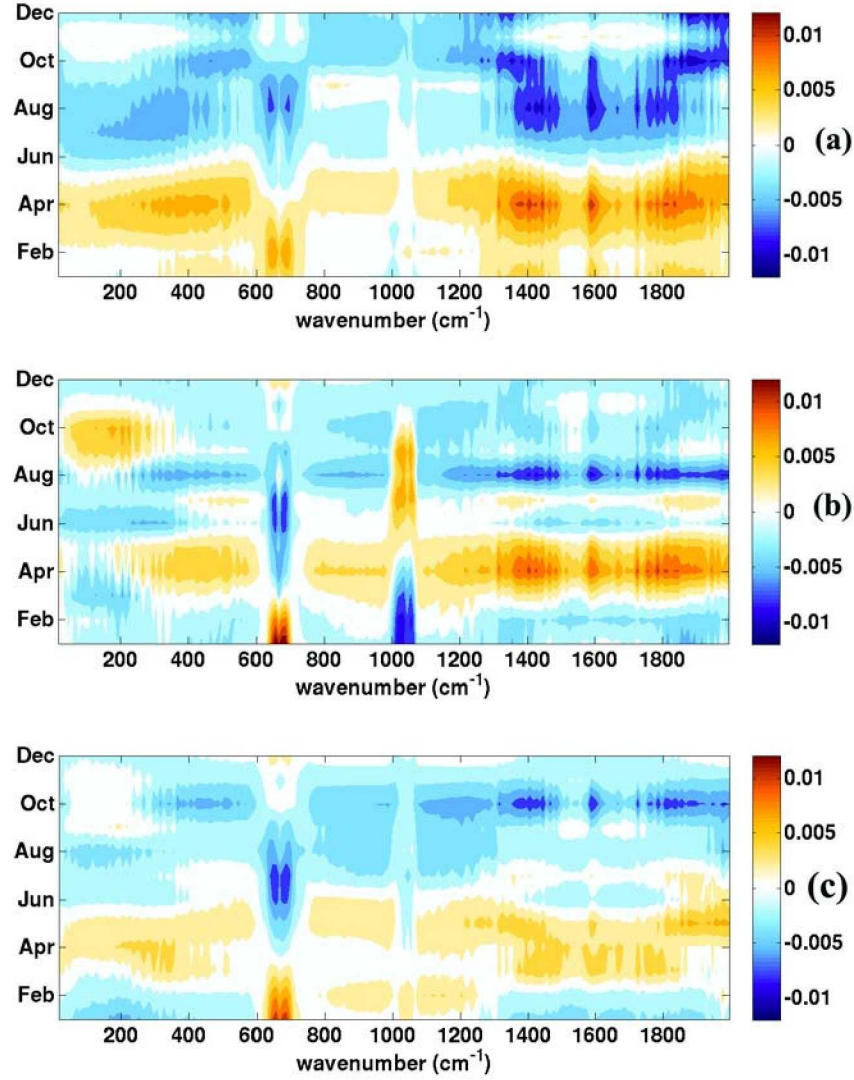


Figure 10. (a) The AM2 monthly deviations (anomalies) of the clear-sky spectral greenhouse parameters  $g_{\Delta\nu}$  (per  $10\text{cm}^{-1}$  interval) from the annual mean  $g_{\Delta\nu}$  (the solid line in Figure 9b) as computed from MODTRAN<sup>TM</sup>-5. (b) Same as (a) except for the  $g_{\Delta\nu}$  derived from collocated AIRS and CERES observations. (c) Same as (a) except for the 2004 NCEP-DOE reanalysis 6-hourly output. The 6-hourly NCEP-DOE reanalysis is processed in a way similar to the AM2 output.